Collisional-radiative modeling of the L-shell emission of Mo^{30+} to Mo^{33+} emitted from a high-temperature–low-density tokamak plasma

K. B. Fournier* and W. H. Goldstein
Lawrence Livermore National Laboratories, P.O. Box 808, Livermore, California 94550

D. Pacella and R. Bartiromo
Associazione EURATOM-Comitato Nazionale per la Ricerca e per lo Sviluppo dell'Energia Nucleare e delle Energie Alternative, sulla Fusione, Centro Ricerche Energetiche della Casaccia Frascati, Cassella Postale 65-00044, Frascati, Italy

M. Finkenthal† and M. May
Johns Hopkins University, Department of Physics and Astronomy, Baltimore, Maryland 21218
(Received 26 June 1995; revised manuscript received 15 September 1995)

The x-ray spectra of several highly stripped molybdenum ions have been recorded between 0.6 and 5.5 Å in the Frascati tokamak upgrade with a rotating crystal spectrometer. Detailed, quasi-steady-state collisional-radiative models have been used to interpret emission features from inner shell, electron impact excitations in molybdenum ions near the neonlike charge state and to characterize the charge state distribution in the plasma. Processes such as resonant excitation, excitation autoionization, and dielectronic recombination have been included in the models of the molybdenum ions' emission features. Introducing the excitation-autoionization process into ionization equilibrium calculations brings agreement between observations and calculations of the relative ionization equilibrium fractions of highly stripped molybdenum ions. Absolutely calibrated spectra and detailed models for the excitation processes in these molybdenum ions allow us to calculate crucial plasma parameters, such as the concentration of impurity ions in the plasma and the amount of power lost from the plasma through impurity line radiation.

PACS number(s): 52.25.Vy, 32.70.Fw, 32.30.Rj

I. INTRODUCTION

Molybdenum is currently being used as a limiter material on the Frascati tokamak upgrade (FTU) [1] and as the first wall material in the Alcator C-Mod Tokamak (Plasma Fusion Center, Massachusetts Institute of Technology) [2]. Consequently, the presence of molybdenum ions in these plasmas is unavoidable. Spectroscopic observations in the vacuum ultraviolet (VUV) and x-ray spectral regions are necessary to diagnose the plasmas's impurity density distributions [3]; furthermore, spectroscopic observations of impurity radiation enable one to understand bulk plasma properties such as impurity transport and radiative cooling of the central plasma [4]. In future generations of reactors, such as the International Thermonuclear Experimental Reactor (ITER), molybdenum and tungsten are being considered as possible candidates for the divertor target material in order to minimize erosion; the understanding of the behavior of medium and heavy atoms in a hot plasma will therefore be essential for the successful operation of large fusion devices [5].

L-shell x-ray transitions in molybdenum ions were first observed in tokamak plasmas by Rice *et al.* at Alcator with spectral resolution comparable to that of the current experiments [6]. A comparison in Ref. [6] of calculated oscillator strengths with observed emission features demonstrated that such techniques are excellent to classify atomic transitions, but are not adequate for predicting the brightness of an emission feature from an ion in the high-temperature, low-density tokamak plasma. High resolution L-shell x-ray spectra of molybdenum ions emitted from the Alcator-C tokamak plasma were further investigated by Källne, Källne, and Cowan [7]. In their paper, identifications were made for many Mo^{31+}, Mo^{30+}, and Mo^{29+} lines. The work in Ref. [7] also uses approximations for dielectronic satellite intensities and rough excitation physics to estimate the amount of cooling the plasma undergoes through line radiation. In the current work, we have used detailed collisional-radiative (CR) models to explain the observed intensity of L-shell x-ray emission features of highly stripped molybdenum recorded in the Frascati tokamak upgrade.

In the work presented below, we use *ab initio,* fully relativistic atomic structure data and distorted wave collisional excitation rates to generate a synthetic spectrum for each ion. The spectrum of each ion is weighted according to a detailed ionization balance model that differs substantially from the coronal ionization equilibrium cal-

*Johns Hopkins University, Department of Physics and Astronomy, Baltimore, MD 21218.
†Permanent address: Racah Institute of Physics, Hebrew University, Jerusalem, Israel.

culations used in Refs. [6] and [7]. We note that the authors of Ref. [7] had to adopt semiempirical relative abundances of different charge states to obtain good agreement between models and observations of molybdenum line intensities; the conclusion in Ref. [7] is that the ratio of ionization to dielectronic recombination rates is larger than calculated. In Sec. III, below, we present calculations of the rate of excitation autoionization for highly stripped molybdenum ions; the inclusion of excitation-autoionization rates in the ionization equilibrium calculations brings excellent agreement between the current models and observations of molybdenum emission features. This model leads to an estimate of the total molybdenum concentration in the plasma and the power lost from the plasma due to line radiation. The high quality of the atomic physics data, and the later ionization equilibrium models, allow us to analyze the FTU plasma from a single ion's spectrum.

II. EXPERIMENTS

FTU is a compact, high field tokamak [8] with major radius $R=0.935$ m, minor radius $a=0.3$ m, toroidal field $B_t \leq 8$ T, and plasma current $I_p \leq 1.4$ MA, with the ability to operate over a wide range of densities $[(0.3-3.0)\times 10^{20}\ \mathrm{m}^{-3}]$. The plasma discharges under investigation in the present work last about 1.5 s, have standard parameters $B_t \cong 6$ T and $I_p \leq 0.8$ MA, densities in the range $(0.4-2.0)\times 10^{20}\ \mathrm{m}^{-3}$, electron temperatures in the core of 1.0–2.8 keV, and ohmic input power ≤ 1.5 MW. The vacuum chamber is made of stainless steel AISI 304, and the circular cross section of the plasma is defined by a poloidal limiter formed by Mo mushrooms mounted on a steel support. After a suitable wall conditioning procedure [1] and cooling the chamber to a working temperature of 77 K (liquid nitrogen), the machine maintains a low level of oxygen and metallic impurities (Cr, Fe, Ni, and Mo). The principal mechanism of impurity production in the FTU is sputtering of the limiter material; for ions in the core of the plasma, confinement times are long, and plasma transport does not effect the ion distributions.

The spectrometer built for the present experiment uses a simple Bragg configuration with a rotating crystal and an extended detector [9]; its layout is shown in Fig. 1. The detector is formed by three stacked multiwire proportional chambers (MWPC's), and allows the discrimination of different orders of diffraction by exploiting the different detection efficiency of each chamber [9]. MWPC's were chosen because they have high and predictable efficiency, and can operate at high counting rates (exceeding 1 MHz). Details of the device's design and calibration can be found in Ref. [9].

A mosaic graphite crystal was chosen for this experiment for its high reflectivity and its suitability for the energy range. Its plane spacing $2d=6.708$ Å yields a wavelength range of 0.6–5.5 Å $[2.3<E(\mathrm{keV})<20]$. The collimator, designed in accord with the low resolution crystal, has an angular divergence of 5.3×10^{-3} rad. The resulting resolving power in the region of interest for these experiments is approximately $\lambda/\Delta\lambda \leq 200$.

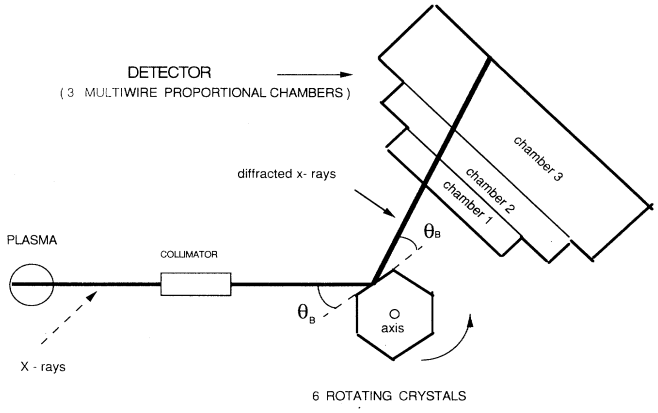

FIG. 1. The experimental setup for recording x-ray spectra on the Frascati tokamak upgrade.

The total luminosity of the spectrometer is given by the contributions of collimator, crystal, and detector. The spectrometer, in the absence of plasma disruptions or intense runaway electron production, has a very high signal to noise ratio with a wide dynamic response (almost two orders of magnitude in the same plasma discharge). In plasmas produced at FTU, we record high fluxes $[10^{12}-10^{14}$ photons/(s cm^2)], and consequently achieve good time resolution (about 1 ms for a line transition).

In Fig. 2 a full range spectrum, not yet corrected by the luminosity curve of the apparatus, is shown. The sharp step at $\lambda=3.89$ Å is caused by the K_β absorption edge of the argon gas used in the detector chambers [9], and produces a large variation in the efficiency of the first detection chamber. This edge can be used as an absolute reference point for the wavelength scale.

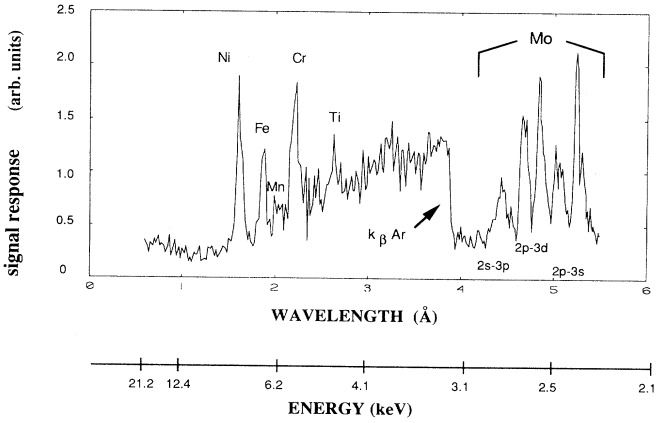

FIG. 2. The full range spectrum taken with the spectrometer described in this paper, not corrected for the apparatus's luminosity function. This spectrum shows the metallic, intrinsic impurities in the plasma as well as the continuum background, and the $K\beta$ edge of argon, which can serve as a wavelength standard.

III. ATOMIC STRUCTURE CALCULATIONS AND COLLISIONAL RADIATIVE MODELS

Ab initio atomic structure data for Mo^{29+} (Al I-like) to Mo^{33+} (F I-like) (ground states $2p^6 3s^2 3p$ to $2s^2 2p^5$, respectively) have been generated using the HULLAC package. HULLAC generates atomic wave functions using the fully relativistic, parametric potential code RELAC [10]. The package includes ANGLAR, which uses the graphical angular recoupling program NJGRAF to generate fine structure levels in a *jj*-coupling scheme for a set of user-specified electron configurations [11]. RELAC then calculates energy levels and transition probabilities.

Atomic transition rates (detailed below), and the energy level structure generated from the configurations listed in Table I, are used to construct the collisional-radiative rate matrix

$$\frac{dn_j}{dt} = \sum_i n_i R_{i\to j} - n_j \sum_i R_{j\to i} \ , \tag{1}$$

where n_j is the population in level j, and $R_{i\to j}$ is the total rate for transitions between levels i and j. The relative ground state populations for all the charge states in the model at a given temperature and density were found by an independent ionization balance calculation: once the ground state populations were known, they were entered into Eq. (1), and the level populations for the excited states in each ion were found. This technique assumes the quasi-steady-state (QSS) approximation in which the excited state populations equilibrate much faster than time scales for changes in the plasma conditions or in the ground state populations [12,13].

In calculating the x-ray spectra of Mo^{29+} to Mo^{33+}, careful attention has been paid to accounting for configuration interaction (CI) effects on level energies and transition rates through the inclusion of doubly excited states, where appropriate, in the structure calculation for each ion (see Table I). For construction of the synthetic spectrum of the Frascati plasma, we have considered all electric and magnetic dipole and quadrupole ($E1$, $E2$, $M1$, and $M2$, respectively) transitions possible between all the energy levels in the model. Table II lists the transitions of Mo^{32+} which are of interest in the present experiment. The table lists, from left to right, a label for the dipole transitions, conforming to a conventional naming scheme in the Ne I-like isosequence [14], the atomic transition in *jj*-coupled notation, and the calculated transition rate for each listed decay. The upper states are designed by two orbitals specifying the hole in the $n=2$ shell and the occupied orbital in the $n=3$ shell. Electric and magnetic quadrupole transitions are labeled in order of increasing wavelength as $E21$, $E22$, and $M2$.

The factorization theorem of Bar-Shalom, Klapisch, and Orge [15] makes possible the fast, accurate calculation of the distorted wave approximation (DWA) electron-impact excitation rates between all levels of each charge state mentioned above. This capability is offered in the CROSS [15] part of the HULLAC package. It has been shown that for Ne I-like ions, the process of resonant excitation [16] can contribute substantially to the total excitation rate from the ground state to an excited state with a $2p$ hole. Chen and Reed [16] have computed

TABLE I. Configurations used in the structure calculations of Mo^{29+} to Mo^{33+}.

Mo^{29+}		Mo^{30+}	
$2s^2 2p^6 3s 3l 3l'$	$(l=s,p,d\ \ l'=p,d)$	$2s^2 2p^6 3l 3l'$	$(l,l'=s,p,d)$
$2s^2 2p^6 3s 3l 4l'$	$(l=s,p\ \ l'=s,p,d,f)$	$2s^2 2p^6 3l 4l'$	$(l=s,p,d\ \ l'=s,p,d,f)$
$2s^2 2p^5 3s^2 3p 3l$	$(l=p,d)$	$2^2 2p^5 3s 3l 3l'$	$(l,l'=s,p,d)$
$2s^2 2p^5 3s^2 3p 4l$	$(l=s,p,d,f)$	$2s^2 2p^5 3s^2 4l$	$(l=s,p,d,f)$
$2s 2p^6 3s^2 3p 3l$	$(l=p,d)$	$2s 2p^6 3s^2 3l$	$(l=s,p,d)$
$2s 2p^6 3s^2 3p 4l$	$(l=s,p,d,f)$	$2s 2p^6 3s^2 4l$	$(l=s,p,d,f)$
Mo^{31+}		Mo^{32+}	
$2s^2 2p^6 3l$	$(l=s,p,d)$	$2^2 2p^6$	
$2s^2 2p^6 4l$	$(l=s,p,d,f)$	$2s^2 2p^5 3l$	$(l=s,p,d)$
$2s^2 2p^5 3l 3l'$	$(l,l'=s,p,d)$	$2s^2 2p^5 4l$	$(l=s,p,d,f)$
$2s^2 2p^5 3s 4l$	$(l=s,p,d,f)$	$2s 2p^6 3l$	$(l=s,p,d)$
$2s 2p^6 3l 3l'$	$(l,l'=s,p,d)$	$2s 2p^6 4l$	$(l=s,p,d,f)$
$2s 2p^6 3s 4l$	$(l=s,p,d,f)$		
Mo^{33+}			
$2s^2 2p^5$			
$2s 2p^6$			
$2s^2 2p^4 3l$	$(l=s,p,d)$		
$2s^2 2p^4 4l$	$(l=s,p,d,f)$		
$2s 2p^5 3l$	$(l=s,p,d)$		
$2s 2p^5 4l$	$(l=s,p,d,f)$		

this contribution for the $2p^6 \rightarrow (2p_{3/2}, 3s)_2$ $M2$ transition, and found almost a factor of 3 enhancement at 2 keV. Since the DWA calculation of electron-impact excitation rates does not account for resonances, we have augmented the Mo^{32+} DWA collisional excitation rates with the resonant contributions of Chen and Reed [16] for all Mo^{32+} $2p \rightarrow 3s$ and $2p \rightarrow 3p$ transitions from the ground state.

For intermediate Z atoms it is well known that inner shell excited states which lie above the continuum have a large branching ratio toward autoionization [17]. The RELAC code has the capability to calculate the autoionization transition probabilities for any ion in the DWA [18]. We have calculated these rates for all the charge states considered in the present work. Electron-impact ionization rates from both valence and inner subshells have been included using the subshell formulas of Sampson and Golden [19] for each ion. The inverse processes of radiationless capture and three body recombination, respectively, are handled for each ion by detailed balancing of the forward rate. Radiative recombination was found to have a much smaller contribution than dielectronic recombination to the intensity of the satellite lines from Mo^{31+}, Mo^{30+}, and Mo^{29+} to the transition in Table II at the temperatures of interest for this work, and was neglected in the CR models.

Figure 3 compares the predicted coronal ionization equilibrium abundance curves for molybdenum ions near the Ne I-like charge state from an average atom model [20] (upper frame) and the curves calculated in the present work (lower frame). In a coronal plasma, the fractional abundance of a given ion (at equilibrium) is found from

$$\frac{n_{z+1}}{n_z} = \frac{S_z(T_e)}{\alpha_{z+1}(T_e)} , \tag{2}$$

where, for the upper frame of Fig. 3, the ionization rate S_z includes direct, impact ionization, and the recombination rate α_{z+1} includes three-body recombination, radiative, and dielectronic recombination. The charge state distributions in the bottom frame peak at lower temperatures than do those in the upper frame, and the abundance of the filled subshell Ne I-like Mo^{32+} ion is greatly enhanced.

The calculation which produces the curves in the lower frame of Fig. 3 includes the rate of impact excitation of an inner shell electron followed by autoionization (EA) in the ionization rate in Eq. (2) for the charge states Mo^{28+} to Mo^{32+}. The EA rate is given by

$$S_i^{\mathrm{EA}}(T_e) = \sum_j Q_{ij}(T_e) B_j^{\mathrm{auto}} \tag{3}$$

where $Q_{ij}(T_e)$ is the electron-impact excitation rate found from CROSS [15] for the state i to an intermediate state j above the ionization limit, and B_j^{auto} is the branch-

TABLE II. *L*-shell x-ray transitions in Ne I-like molybdenum. The upper states of transitions are labeled by two orbitals: the first the inner shell hole, and the second the occupied orbital of the upper state; subshells are designated by + for $l+s$ and − for $l-s$ couplings, and the total J value of the state is written after the orbitals as a subscript. The calculated transition rates are from RELAC; the numbers in parentheses indicate powers of 10.

	Mo^{32+} transitions	
Label	Transition	A_{ij} (s^{-1})
3*A*	$2s^22p^6 \rightarrow (2s+,3p-)_1$	3.567(13)
3*B*	$2s^22p^6 \rightarrow (2s+,3p+)_1$	1.204(13)
3*C*	$2s^22p^6 \rightarrow (2p-,3d-)_1$	1.763(14)
3*D*	$2s^22p^6 \rightarrow (2p+,3d+)_1$	1.815(14)
3*E*	$2s^22p^6 \rightarrow (2p+,3d-)_1$	2.258(11)
3*F*	$2s^22p^6 \rightarrow (2p-,3s+)_1$	7.810(12)
*E*21	$2s^22p^6 \rightarrow (2p+,3p-)_2$	2.563(10)
*E*22	$2s^22p^6 \rightarrow (2p+,3p+)_2$	2.558(10)
3*G*	$2s^22p^6 \rightarrow (2p+,3s+)_1$	1.082(13)
*M*2	$2s^22p^6 \rightarrow (2p+,3s+)_2$	2.908(07)

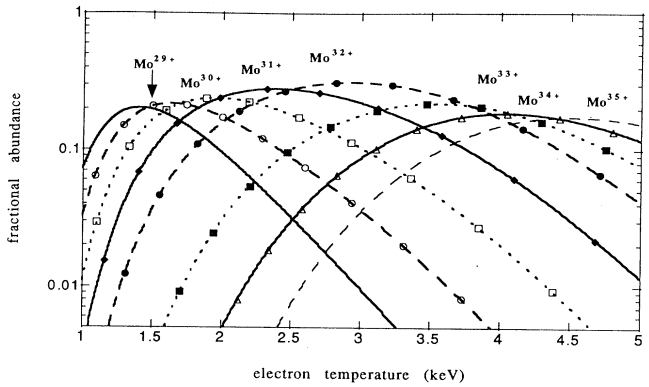

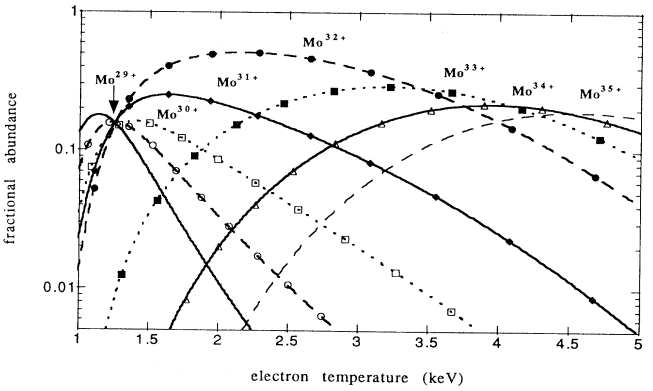

FIG. 3. Ionization equilibrium curves from Eq. (2) for molybdenum charge states expected in the core of the Frascati tokamak upgrade plasmas computed (top) using average-ion models for ionization and semiempirical rates for recombination, and (bottom) including *ab initio* calculations of impact excitation followed by autoionization and replacing the semiempirical rates of dielectronic recombination with *ab initio* rates.

ing ratio for autoionization found using the transition rates of RELAC [10,18] from state j to all possible levels of the next ion. Details of the calculation of the autoionization rates are found in Ref. [18]. For charge states such as the Na I-like Mo^{31+} and Mg I-like Mo^{30+}, the EA process increases the total ionization rate for a given charge state by nearly a factor of 3. Figure 4 shows the quantity

$$R(T_e)=\frac{(S^{\mathrm{DI}}+S^{\mathrm{EA}})}{S^{\mathrm{DI}}}\ , \tag{4}$$

which is the factor by which the ionization rates in Eq. (2) are enhanced by the inclusion of the EA process. An additional enhancement of a factor of 2 is found for the total ionization rate, giving rise to the bottom set of curves in Fig. 3 (for a total enhancement of a factor of 6 for the ionization rate for Na I-like Mo^{31+} between the top and bottom sets of curves in Fig. 3) by replacing the semiempirical impact ionization rates of Ref. [20] with the ionization rates calculated using the formulas in Ref. [19].

The dominant recombination mechanism for molybdenum in the plasmas under consideration is dielectronic recombination (DR); the low density tokamak plasmas make the three-body recombination process negligible, and, at the temperatures relevant to the observed charge states, DR rates exceed radiative recombination rates by an order of magnitude. The widely used, semiempirical Burgess-Merts formula [21,22] for DR is used in calculating the upper curves of Fig. 3. *Ab initio* calculation of the DR rates for Mo^{33+} to Mo^{29+} have been performed using RELAC; the RELAC calculation uses the detailed level energies of all doubly excited states of the recombined ion, and the fully relativistic, intermediate-coupled calculation of radiative stabilization and autoionization rates. The methodology used in the calculation of the rate coefficients in the present work has been described elsewhere [23].

Figure 5 shows the percentage difference between the DR rates computed in the present work and those found from the Burgess-Merts formula (used in the upper curves in Fig. 3); the *ab initio* rates are seen to be larger than the Burgess-Merts rates. Figure 5 is divided vertically by a dotted line at an electron temperature of 1 keV. In the region below 1 keV, the difference between the two calculations is large, reaching several thousand percent at the lowest temperatures. In this temperature region, the

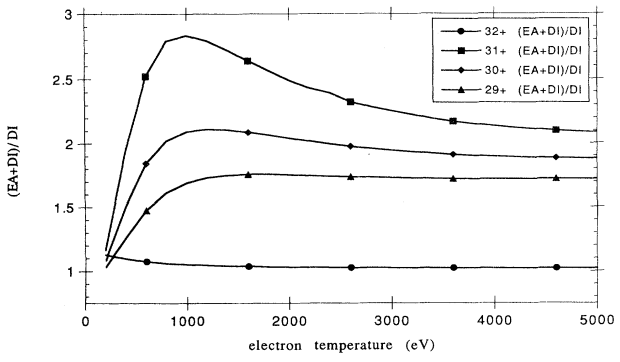

FIG. 4. The factor from Eq. (4) by which impact ionization (DI) rates are augmented when excitation autoionization (EA) is included in the total ionization rate for Mo^{29+}, Mo^{30+}, Mo^{31+}, and Mo^{32+} in Eq. (2).

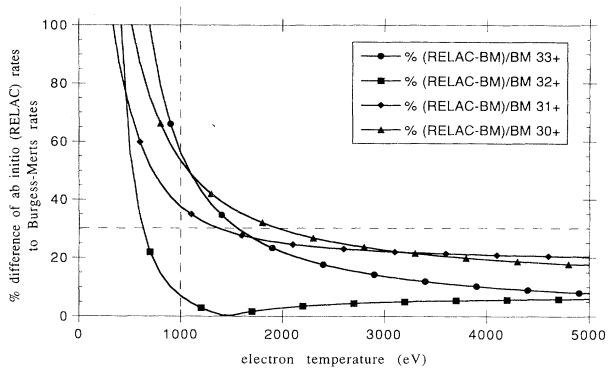

FIG. 5. The percentage by which the *ab initio* dielectronic recombination rates computed for this paper differ from the semiempirical rates given by the Burgess-Merts formula for Mo^{30+}, Mo^{31+}, Mo^{32+}, and Mo^{33+}.

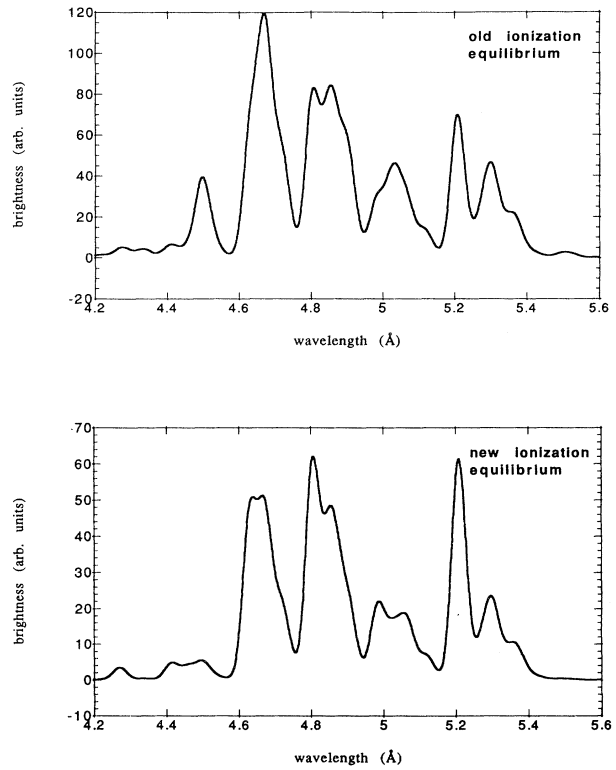

FIG. 6. (Top) CR spectrum from Eq. (1) for Mo^{29+} to Mo^{3+} calculated using the ionization equilibrium abundance curves in the upper frame of Fig. 3. (Bottom) same as upper frame, but calculated using the ionization equilibrium abundance curves in the lower frame of Fig. 3. Each feature has been given a Gaussian linewidth equal to that of the spectrometer described in Sec. II.

dominant DR channel is through $\Delta n=0$ captures ($2l \rightarrow 2l'$ for Mo^{33+}, $3l \rightarrow 3l'$ for Mo^{31+}, and Mo^{30+}); the detailed *ab initio* structure calculations done with RELAC indicate that these rates fall off rapidly within increasing temperature. In the range above 1 keV, the dominant recombination mechanism is through $\Delta n=1$ transitions ($2l \rightarrow 3l'$, $3l \rightarrow 4l'$); here the two calculations differ by less than 30%.

Figure 6 compares the CR spectra of Mo^{29+} to Mo^{33+} predicted along a line of sight through the core of a typical FTU plasma constructed using the two ionization equilibrium abundance calculations contrasted in Fig. 3. The effect of changing the charge state distribution in the plasma is dramatic; the average atom model enhances the satellite transitions to the Ne I-like Mo^{32+} lines listed in Table II. Hence the center of gravity of each feature in the upper frame of Fig. 4 is at a longer wavelength than the corresponding feature in the lower frame. In summary, the ion fractions shown in the lower set of curves in Fig. 3 have been used in the QSS-CR models of Eq. (1). The introduction of EA rates into Eq. (2) results in the shifting of the Al I-, Mg I-, and Na I-like ions to cooler temperatures; the fact that these ions are burned through at a lower temperature means the Ne I-like Mo^{32+} ion appears at a lower temperature, and in greater abundance. The results of applying the ionization equilibrium models in Eq. (1) are seen in Fig. 6, and applied to experiments done on the FTU in Secs. IV and V below.

IV. ANALYSIS OF REPRESENTATIVE SPECTRA

The top frame of Fig. 7 shows a spectrum taken during a standard, limited discharge on the FTU. The characteristics for the steady-state part of the plasma during this shot are a central electron temperature of 1.8 keV and a central electron density of 1.4×10^{14} cm^{-3}. The emission was recorded in a scan lasting about 5 m. The bottom frame in Fig. 7 is a simulated spectrum along a line of sight passing through a plasma with electron temperature and density profiles shown in Fig. 8. The dotted trace in Fig. 7 was obtained by folding the simulated line emission with a Gaussian representing the instrumental linewidth of the spectrometer used in this experiment. The Ne I-like transitions from Table II are labeled in the conventional manner in the bottom frame of Fig. 7; the corresponding spectral feature in the top frame of Fig. 7 has been designated by a letter indicating the dominant Ne I-like transition contributing to the feature. Two exceptions to this scheme are the features labeled *b*12, which corresponds to the Mo^{32+} *E*22 transition and satellites, and $G+M2$, which has the Mo^{32+} 3*G* and *M*2 transitions as components.

Table III lists the observed and calculated intensities for the spectral features in Fig. 7, and compares observed and calculated wavelengths for the strongest transitions which contribute to the observed emission features. Observed wavelengths are from high resolution observations by Källne, Källne, and Cowan in Ref. [7]. The 3*C* 3*D*, and $3G+M2$ Ne I-like transitions listed in Table II clearly dominate the spectrum; satellite transitions to the

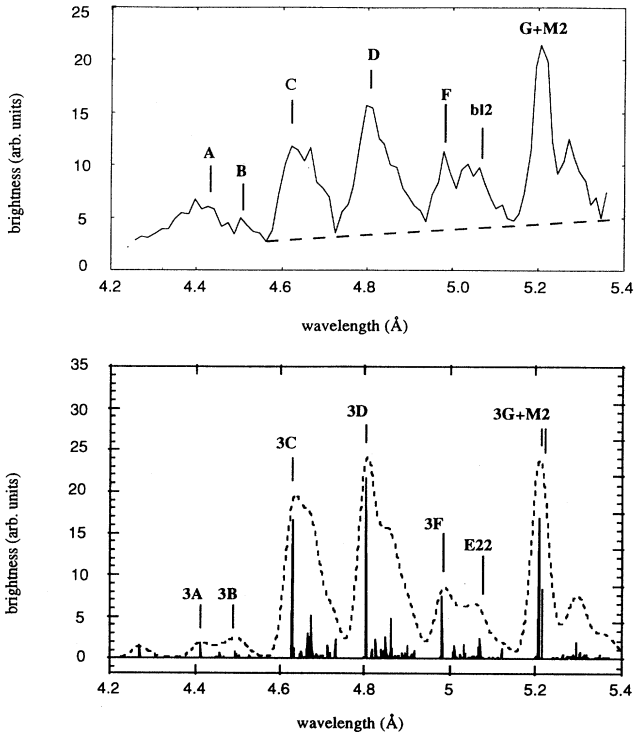

FIG. 7. (Top) Experimentally recorded spectrum from a FTU plasma with a molybdenum limiter. The plasma has a core electron temperature of 1.8 keV and an electron density of 1.4×10^{14} cm^{-3}. Labeled features are identified in Table III. (Bottom) Collisional-radiative spectrum calculated with electron temperature and density parameters the same as those along the line of sight of the spectrum in the top frame. The solid lines are the QSS-CR brightness of the Mo^{29+} to Mo^{33+} features, the dashed envelope is the spectrum made from convoluting each feature after giving it a Gaussian linewidth equal to that of the experimental device.

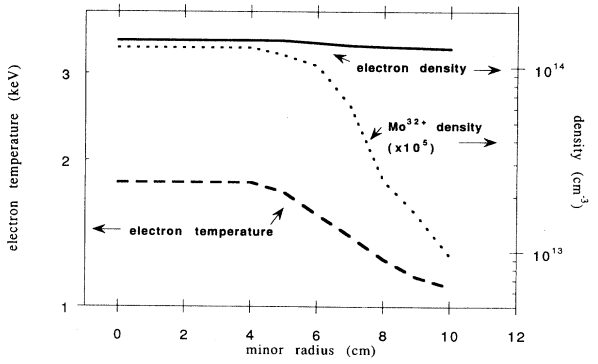

FIG. 8. The measured electron temperature profile in keV (dashes, left axis) and electron density profile in cm^{-3} (solid line, right axis) for the steady state phase of the plasma recorded in Fig. 7. The dotted curve is the Mo^{32+} density profile (multiplied by 10^5) as calculated from Eq. (6).

Ne I-like features are quite strong, and have been included in Table III. The agreement between the measured [7] and calculated wavelengths for all transitions is quite good.

For the features in the top frame of Fig. 7, the observed intensity is listed on the same line as the feature's label in Table III. The observed intensity is found by integrating the area (after subtracting the straight line background profile shown by a dotted line) under each feature, which includes the contribution from the Ne I-like transition and blending from the adjacent satellite lines, and normalizing the result to the intensity of the feature labeled *D*. The theoretical intensity, computed by integrating the area under each feature in the synthetic line-of-sight spectrum, is also given. The strong constituents of each spectral feature labeled in the top of Fig. 7 are listed below that figure's label in Table III.

The match between the observed intensities and the

TABLE III. Comparisons between observed (Ref. [7]) and calculated (present work) transition wavelengths for Mo^{30+} to Mo^{33+}, and observed and calculated transition intensities (both, present work) for *L*-shell x-ray features. The labels for Ne I-like transitions are the same as listed in Table II. The physical state of the upper level of a satellite transition is named for the dominant *jj*-coupled basis function in the actual, multiconfiguration state. The upper states in the satellite transitions in this table are indicated by a series of *jj*-coupled orbitals representing, first, an inner shell vacancy; second, any spectator electrons (e.g., the $3s^2$ electrons in Mo^{30+}); and third, the excited orbital to which the inner shell electron is promoted. The lower state in each transition is indicated by a list of filled subshells and one or more valence orbitals (in the case of more than one, the valence orbitals are indicated by + and − as in Table II).

Label	ion	Constituents transition	λ^{obs} [a] (Å)	λ^{ther} (Å)	I^{obs} (arb. units)	I^{ther}
A					*blend*	9
	32+	$3A$ [b]	4.412	4.412		
B					*blend*	4
	32+	$3B$ [b]	4.458	4.459		
C					64	58
	32+	$3C$ [b]	4.630	4.629		
	31+	$2s^22p^63s \rightarrow (2p_-, 3s, 3d_+)_{3/2}$	4.635	4.634		
	33+	$2s^22p^5_+ \rightarrow (2p_+, 3d_+)_{5/2}$		4.651		
	33+	$2s^22p^5_+ \rightarrow (2p_+, 3d_-)_{3/2}$		4.664		
	31+	$2s^22p^63s \rightarrow (2p_-, 3s, 3d_-)_{1/2}$	4.664	4.665		
	31+	$2s^22p^63s \rightarrow (2p_-, 3s, 3d_-)_{3/2}$	4.668	4.671		
	30+	$2s^22p^63s^2 \rightarrow (2p_-, 3s^2, 3d_-)_1$	4.680	4.674		
	33+	$2s^22p^5_+ \rightarrow (2p_+, 3d_+)_{5/2}$		4.678		
D					100	100
	32+	$3D$ [b]	4.804	4.803		
	31+	$2s^22p^63s \rightarrow (2p_+, 3s, 3d_+)_{1/2}$	4.825	4.826		
	31+	$2s^22p^63s \rightarrow (2p_+, 3s, 3d_+)_{3/2}$	4.837	4.840		
	31+	$2s^22p^63s \rightarrow (2p_+, 3p_+, 3p_+)_{3/2}$ [c]	4.846	4.849		
	30+	$2s^22p^63s^2 \rightarrow (2p_+, 3s^2, 3d_+)_1$	4.869	4.863		
	31+	$2s^22p^63s \rightarrow (2p_+, 3s, 3d_-)_{1/2}$		4.864		
F					30	20
	32+	$3F$ [b]	4.982	4.982		
*bl*1					*blend*	5
	32+	$(E2) \quad E21$ [b]		5.008		
	33+	$2s^22p^5_+ \rightarrow (2p_+, 3s)_{3/2}$		5.026		
	30+	$2p^6(3s3p_-)_1 \rightarrow (2p_-, 3s^2, 3p_-)_0$		5.033		
	33+	$2s^22p^5_+ \rightarrow (2p_+, 3s)_{5/2}$		5.037		
	31+	$2p^63p_+ \rightarrow (2p_-, 3s, 3p_-)_{1/2}$		5.066		
*bl*2				5.071	*blend*	10
	32+	$(E2) \quad E22$ [b]		5.071		
	33+	$(2s2p^6)_{1/2} \rightarrow (2s, 2p^5_+, 3s)_{3/2}$		5.077		
	30+	$2p^6(3s3p_+)_1 \rightarrow (2p_-, 3s^2, 3p_-)_0$		5.122		
$G+M2$					79	61
	32+	$3G$ [b]	5.207	5.207		
	32+	$(M2) \quad M2$ [b]	5.217	5.216		

[a] As reported in Ref. [7].

[b] As identified in Table II.

[c] Enabled by wave-function mixing: $2p^63s \rightarrow [(2p^53p^2)_{3/2} + (2p^53s3d)_{3/2}]$.

theoretical intensities of the emission features is, overall, very good. The feature corresponding to $3F$ is observed to be 50% brighter than it is predicted to be. This transition is strongly blended with the near by $E21$ and $E22$ transitions and related satellite lines, and is, therefore, problematic. Analysis of the population flux channels [from Eq. (1)] into and out of upper states of the $3F$, $3G$, and $M2$ transitions reveals that only 10% of the population in these levels comes directly from the ground state; the majority of the population feeding these transitions arrives from radiative cascades from the $2p^5 3p$ levels. Because our models neglect population flux channels from radiative recombination into the excited states of Mo^{32+}, there is a greater uncertainty in the modeled brightness of the $2p \rightarrow 3s$ ($3F$, $3G$, and $M2$) transitions than in the $2P \rightarrow 3d$ transitions which are fed almost exclusively by collisional excitations directly from the ground state.

Finally, the contribution from other metallic impurities to the measured brightness of any molybdenum feature in Fig. 7 has been assessed using the known, absolute calibration of the spectrometer up to the third order of diffraction [9]. Nearly 50% of the measured brightness of feature A (indicated by *blend* in Table III) comes from the chromium K-α transition at 2.2 Å in second order (cf. Fig. 2). The K-α transition of titanium at 2.65 Å in second order is responsible for a 20% brightness enhancement of the emission at 5.3 Å.

V. ANALYSIS OF IMPURITY CONCENTRATIONS

The photometrically calibrated spectra taken on FTU in the present experiments provide an estimate of the total concentration of molybdenum ions in the plasma. The feature labeled D in Fig. 7 has an absolute brightness of 4×10^{14} photons/(sec sr cm^2) when integrated in wavelength. We assume that at least 85% of this flux is from the Mo^{32+} $3D$ line. Figure 8 shows the measured electron temperature profile (dashes) and electron density profile (solid line) for the plasma giving rise to the spectrum in Fig. 7. [The CR models reveal that (in the quasi-steady-state) over 95% of the population in the upper state of the 3D transition arrives there by direct electron-impact excitation from the ground state]. The density of Mo^{32+} ions necessary to give us the brightness of the observed feature is found according to

$$B_D^{\rm Obs}=\frac{\varepsilon}{4\pi}\int_{-L}^{+L} n_e(x)n_{\rm Mo}^{32+}(x)Q_{g,3D}(x)dx \ , \tag{5}$$

where $B_D^{\rm Obs}$ is the observed brightness of the feature labeled D in Fig. 7, $Q(x)$ is the excitation rate coefficient from the ground state to the upper state of the 3D transition, $n_e(x)$ and $n^{Z+}(x)$ are the local electron and charge state densities, respectively, ε is the branching ratio for the transition, and the integral is along the line of sight in the plasma. Figure 8 also shows the spatial profile (multiplied by 10^5 to be visible on the density axis) of the Mo^{32+} ion (dots) derived from Eq. (5). From our ionization balance models, the density of Mo^{32+} ions at a given temperature can be related to the total molybdenum density in the plasma according to

$$n_{\rm Mo}^{32+}(T_e)=f^{32+}(T_e)n_{\rm Mo} \ , \tag{6}$$

where $f^{z+}(T_e)$ is the fractional abundance of a given charge state at a given temperature (see the lower frame of Fig. 3), and $n_{\rm Mo}$ is the total molybdenum density. We find a total density of molybdenum of 3.2×10^{10} cm^{-3} for the representative discharge in Fig. 7. By dividing this density by the chord-averaged core electron density, 1.3×10^{14} cm^{-3}, we find a concentration of molybdenum in the FTU plasma of between two and three parts per 10 000. For the sake of comparison, the upper set of curves in Fig. 3 yields a total molybdenum density of 4.6×10^{10} cm^{-3}, which implies a concentration of four parts per 10 000. As discussed below, experimental measurements of the effective charge of the plasma and the total power radiated by impurity ions confirm the former calculation, made with the lower set of curves in Fig. 3.

A quantitative check of the derived molybdenum density for the discharge in Fig. 7 can be obtained by considering the measured effective charge and radiation losses from the central region of the plasma. Since $Z_{\rm eff}$ and radiated power in the core depend strongly on molybdenum density, when measured independently of models of molybdenum distributions they are reliable experimental checks of the molybdenum density deduced spectroscopically from the detailed CR model described above. To obtain precise information, one must consider the contribution of other impurities to the observed values of the effective charge and radiation losses. The K-α transitions of the He-like ions of iron, nickel, manganese, chromium, and titanium appear in the full range spectrum of Fig. 2. Given the excitation cross section for these lines [24], and the absolute luminosity of the spectrometer, the K-α transitions of the metallic ions Fe, Ni, and Cr are used to derive the core-averaged densities of these ions. We obtain

$$n_{\rm Fe}=1.8\times10^{10} \text{ cm}^{-3} \ ,$$
$$n_{\rm Ni}=1.1\times10^{10} \text{ cm}^{-3} \ ,$$
$$n_{\rm Cr}=5.0\times10^{9} \text{ cm}^{-3} \ ,$$

the other metallic ions being negligible. Spectroscopic measurements of emission visible up to VUV show that oxygen is the most abundant of low Z impurities in the discharge considered. Its density, $n_O=3.8\times10^{11}$ cm^{-3}, can be deduced from the enhancement of the continuum level of the spectrum of Fig. 2 with respect to the hydrogenic bremsstrahlung [24].

The effective charge of the plasma can be found without relying on models for impurity distribution in the plasma by measuring visible bremsstrahlung emission or plasma resistivity [4]. The effective ionic charge of the plasma is defined as

$$Z_{\rm eff}=\sum_{Z,A}\frac{n_A^Z Z^2}{n_e} \ , \tag{7}$$

where n_A^Z is the density of charge state Z^+ of atom A, and the sum is taken over all charge states present of all

impurity atoms in a local region. Based on the above-derived impurity densities for other metallic impurities, and the spectroscopically derived molybdenum density described above, the contributions of the different impurity ions (molybdenum, iron, nickel, chromium, and oxygen, respectively) to the calculated value of the effective charge Z_{eff} in the plasma core are

$$Z_{\text{eff}} = 1 + 0.20 + 0.08 + 0.05 + 0.02 + 0.19 = 1.54 \, . \quad (8)$$

This is in reasonable agreement, given theoretical and experimental uncertainties, with the value of 1.45 (± 0.05) obtained independently from the measurement of the visible bremsstrahlung emissions and the plasma resistivity.

The total radiated power from impurity ions in the plasma's core can be obtained by Abel inversion of chord-integrated bolometric measurements. Preliminary calculations of radiative loss rates from line emission by molybdenum in a low density plasma using the charge state distributions in the lower frame of Fig. 3 and the calculated line emissivities for all molybdenum charge states from detailed, QSS collisional radiative models has been undertaken, and will be presented elsewhere. We have found that for plasmas between 1.5 and 4 keV, the above models and the widely used cooling rates of Post *et al.* [25] differ by no more than 20%. Hence we use the spectroscopically derived impurity concentrations described in this section and the polynomial fits for generating cooling rates from Post *et al.* [25] to calculate, for a plasma with a core temperature of 1.8 keV and an electron density of 1.3×10^{14} cm^{-3}, a radiation loss from the center of 2.7×10^5 W/m^3 due to molybdenum, 4.5×10^4 W/m^3 due to iron, 4.2×10^4 W/m^3 due to nickel, 1.5×10^4 W/m^3 due to chromium, and 1.0×10^4 W/m^3 due to oxygen, for a total loss of about 3.8×10^5 W/m^3. Comparison with the experimental value of $3.5(\pm 0.5) \times 10^5$ W/m^3 shows very good agreement when one takes into account the theoretical and experimental uncertainties. The ion fractions from the upper set of curves in Fig. 3 indicate a radiation loss in the center of the plasma of 3.9×10^5 W/m^3 from molybdenum, leading to a total loss of nearly 5×10^5 W/m^3, an amount well outside the error allowed by the experimental uncertainty.

VI. CONCLUSIONS

Detailed atomic physics calculations have been put into a quasi-steady-state collisional-radiative model to construct the synthetic spectrum of molybdenum L-shell x-ray radiation. This model spectrum has been compared to the x-ray spectra of highly stripped molybdenum ions in the 2–5-Å range recorded during operation of the FTU when a molybdenum limiter is installed. By modeling the brightness of satellite transitions to the strong $2l - 3l'$ Ne I-like transitions, and by studying the detailed channels by which population arrives in the upper states of the observed transitions, we can calculate the total molybdenum concentration in the plasma and the rate at which the plasma loses energy through impurity radiation. In the future, such cooperation between observations and modeling will be essential to the operation of viable fusion reactors.

ACKNOWLEDGMENT

The present work was performed under the auspices of the U.S. Department of Energy by the Lawrence Livermore National Laboratories under Contract No. W-7405-ENG-48.

[1] F. Alladio *et al.*, Plasma Phys. Control. Fusion **36**, 12B (1994); **36**, 253 (1994).
[2] I. H. Hutchinson *et al.*, Phys. Plasmas **1**, 1511 (1994).
[3] C. DeMichelis and M. Mattioli, Rep. Prog. Phys. **47**, 1233 (1984).
[4] R. C. Isler, Nucl. Fusion **24**, 1599 (1984).
[5] D. Post, R. Hulse, and D. Stotler, Contrib. Plasma Phys. **34**, 300 (1994); J. Cummings, S. Cohen, R. Hulse, D. Post, and M. Redi, J. Nucl. Mater. **176 & 177**, 916 (1990).
[6] J. Rice, E. Marmar, T. Coan, S. Allen, and R. Cowan, Phys. Rev. A **22**, 1 (1980); **22**, 310 (1980).
[7] E. Källne, J. Källne, and R. Cowan, Phys. Rev. A **27**, 2682 (1983).
[8] R. Andreani, Fusion Eng. Design **22**, N1-2 (1993); **22**, 129 (1993).
[9] R. Bartiromo, F. Bombarda, L. Gabellieri, G. Pizzicaroli, A. Tuccillo, and R. Zagarella, Nucl. Instrum. Methods Phys. Res. Sect. B **95**, 537 (1995).
[10] M. Klapisch, Comput. Phys. Commun. **2**, 269 (1971); M. Klapisch, J. L. Schwob, B. S. Fraenkel, and J. Oreg, J. Opt. Soc. Am. **67**, 148 (1977).
[11] A. Bar-Shalom and M. Klapisch, Comput. Phys. Commun. **50**, 375 (1988).
[12] V. A. Boiko, I. Skobelev, and A. Faenov, Fiz. Plazmy **10**, 143 (1984) [Sov. J. Plasma Phys. **10**, 82 (1984)].
[13] D. Bates, A. Kingston and R. McWhirter, Proc. R. Soc. London Ser. A **267**, 297 (1962); **270**, 155 (1962).
[14] M. Loulergue and H. Nussbaumer, Astron. Astrophys. **45**, 125 (1975).
[15] A. Bar-Shalom, M. Klapisch, and J. Oreg, Phys. Rev. A **38**, 1773 (1988).
[16] M. Chen and K. Reed, Phys. Rev. A **40**, 5 (1989); **40**, 2292 (1989).
[17] R. Cowan and J. Mann, Astrophys. J. **232**, 940 (1979).
[18] J. Oreg, W. Goldstein, P. Mandelbaum, D. Mitnik, E. Meroz, J. Schwob, and A. Bar Shalom, Phys. Rev. A **44**, 3 1741 (1991); J. Oreg, W. Goldstein, and M. Klapisch, *ibid.* **44**, 3 (1991); **44**, 1750 (1991).
[19] D. Sampson, L. Golden, and D. Moores, Astrophys. J. **170**, 169 (1971); D. Moores, L. Golden, and D. Sampson, J. Phys. B **13**, 385 (1980); L. Golden, R. Clark, S. Goett, and D. Sampson, Astrophys. J. Suppl. **45**, 603 (1981).
[20] R. Hulse, Nuclear Tech. Fusion **3**, 259 (1983).
[21] A. Burgess, Astrophys. J. **139**, 776 (1964); **141**, 1588

(1965).
[22] A. Merts, R. Cowan, and N. Magee, Los Alamos Scientific Laboratory Report No. LA-6220-MS, 1976 (unpublished).
[23] W. Goldstein, A. Osterheld, J. Oreg, and A. Bar-Shalom, Astrophys. J. **344**, L37 (1989).
[24] E. H. Silver, M. Bitter, K. Brau, D. Eames, A. Greenberg, K. W. Hill, D. M. Meade, W. Roney, N. R. Sauthoff, and S. von Goeler, Rev. Sci. Instrum. **53**, 8 (1982); **53**, 1198 (1982).
[25] D. Post, R. Jensen, C. B. Tarter, W. Grasberger, and W. Lockke, At. Data Nucl. Data Tables **20**, 5 (1977); **20**, 397 (1977).